

# Figure verification of a precision ultra-lightweight mirror: Techniques and results from the SHARPI/PICTURE mirror at NASA/GSFC

Scott Antonille<sup>a</sup>, David Content<sup>a</sup>, Doug Rabin<sup>b</sup>, Shane Wake<sup>a</sup>, Thomas Wallace<sup>a</sup>

<sup>a</sup>Optics Branch, MC551

<sup>b</sup>Solar Physics Branch, MC682

NASA Goddard Space Flight Center, Greenbelt Rd, Greenbelt MD 20771

## ABSTRACT

A high-precision ultra-lightweight 0.5m mirror with ultraviolet grade tolerances on surface figure quality has been measured from its delivery to the Goddard Space Flight Center, through the coating and mounting process, and shown to survive component vibration testing. This 4.5kg, 0.5m paraboloid mirror is the prime optic of two sounding-rocket telescopes: SHARPI (solar high angular resolution photometric imager) and PICTURE (planet imaging concept testbed using a rocket experiment). By integrating the analysis of interferometer data with finite element models, we demonstrate the ability to isolate surface figure effects comparable to UV diffraction limited tolerances from much larger gravity and mount distortions. The ability to measure such features paired with in situ monitoring of mirror figure through the mirror mounting process has allowed for a diagnosis of perturbations and the remediation of process errors. In this paper, we describe the technical approach used to achieve nanometer scale measurement accuracy, we report and decompose the final mounted surface figure of 12.5 nm RMS, and we describe the techniques that were developed and employed in the pursuit of maintaining UV diffraction-limited performance with this aggressively lightweighted mirror.

**Keywords:** lightweight mirror; interferometry; aspheric testing; gravity distortion; mount induced distortion; null optic certification; spaceflight optic verification

## 1. INTRODUCTION

The use of larger, lighter, and more precise space optics requires not only a means of manufacture, but also a means of spacecraft integration and performance verification. We have demonstrated a process capable of producing a high precision mounted lightweight mirror, and we have validated its on-orbit figure. This effort has included the design of a mount capable of surviving the launch environment of a sounding rocket, as well as a mounting process that did not introduce performance degrading figure distortion. Additionally, analysis techniques were developed and adapted to address the challenges in measuring an optic that exceeds its figure specification under the strain of its own weight. Included in this paper are test summaries, lessons learned, a description of our mounting effort, and a brief description of some of the analysis techniques used to accomplish achieve nanometer-level RMS figure uncertainties.

## 2. MIRROR SPECIFICATIONS

The lightweight UV demonstrator mirror delivered by ITT Space Systems is a glass sandwich comprised of a thin faceplate, a waterjet hexagonal core, and a spherical backplate. The mirror was constructed from of Ultra-Low Expansion (ULE) fused silica glass for dimensional thermal stability. With a physical diameter of 55cm and a mass of 4.5kg, it is 92% less massive than a comparably shaped solid. It was delivered to Goddard and measured to have a 0g figure of 9.0nm RMS over spatial periods larger than 5mm. Three invar mount interface pads were bonded to the mirror backplate. The mirror was measured and polished while supported kinematically by tooling balls attached to the three invar mount pads.<sup>1</sup> The lightweight mirror design is summarized in Figure 1a.

The fabrication goals (Fig. 1b) for this lightweight technology demonstrator were specified to show the feasibility of this mirror architecture for diffraction limited applications in the far and extreme ultraviolet (FUV-EUV) bands. ITT demonstrated that this mirror architecture and associated processes could achieve the desired specifications. The delivered figure of 9.0nm RMS, while above the goal, could have been reduced further to meet the 6nm RMS goal but was accepted in lieu of time and cost.

#### Mirror Geometry

Surface Conic Type	Paraboloid
Radius of Curvature (at vertex)	1276.87 mm
Physical Clear Aperture (diameter)	558.8 mm
Optical Clear Aperture (diameter)	508 mm
Inner Obscuration, Physical (radius)	69.9 mm
Inner Obscuration, Optical (radius)	77±2 mm
Mount pad locations (radial)	195.58 mm

#### Lightweighting Geometry

<i>A fused faceplate, lightweighted core, and backplate.</i>		
Core cell shape	Hexagonal	
Cell width (flat to flat)	50 mm	
Cell depth	42.16 mm	
Cell wall thickness	1.2 mm	
Front plate thickness	3.5 mm	
Back plate thickness	2.5 mm	

#### Material and Mass

Material	ULE	
Mass	4.54 kg	
Areal density	19.75 kg/m <sup>2</sup>	
Light weighting*	92 %	

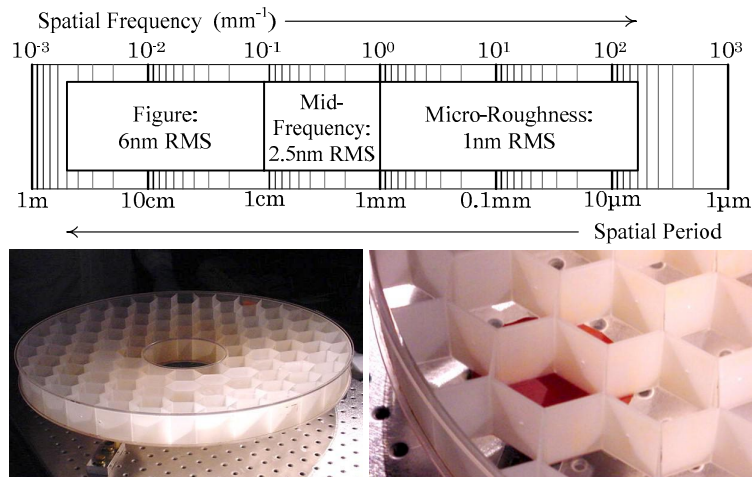


Figure 1. (a) mirror design properties, (b) upper right, figure, mid-frequency, and roughness goals, (c) lower left, uncoated mirror as provided to GSFC, (d) lower right, top view of cell structure over one mounting pad

This high precision demonstrator mirror became associated with two sounding rocket projects that have shared a common front-end telescope design, SHARPI and PICTURE. The Solar High-Angular Resolution Photometric Imager<sup>2</sup> (SHARPI) is proposed to perform 0.1-arcsecond solar imaging in the FUV band, enabling the study of magnetic phenomena on solar scales of 100km. PICTURE<sup>3</sup> (Planetary Imaging Concept Testbed Using a Rocket Experiment) is an extra-solar planetary imaging concept funded by NASA and led by Boston University. The goal of the PICTURE rocket program is to demonstrate deep-nulling coronagraphy capable of imaging  $\epsilon$ -Eridani, a known nearby extra-solar system. Both of these projects require the use of high precision optics in a weightless or “0g” environment and could not afford the weight or cost of a traditional high precision mirror.

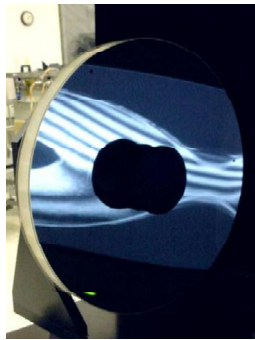
### 3. TECHNICAL APPROACH

The effort at Goddard Space Flight Center focused on the integration and qualification of this mirror in a telescope payload configuration. In particular, our goals were to demonstrate a 0g figure verification compatible with UV diffraction limited performance, to coat the mirror, fabricate a mount and mount the mirror without causing figure distortion, and to perform a vibration qualification of the mounted mirror to sounding rocket requirements at the component level. Once complete, the mirror was integrated into a telescope payload. Throughout our effort, we repeated mirror figure measurements to monitor and characterize shape changes that resulted from our process.

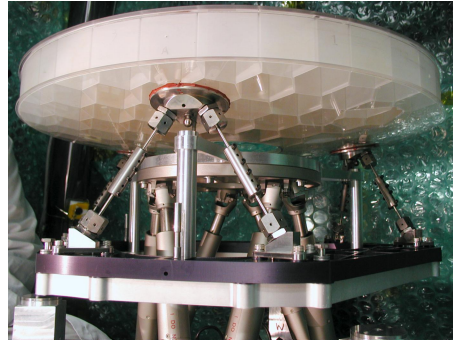
Verifying the surface figure across spatial periods ranging from 10μm to 50cm requires the combination of several techniques best suited to their own particular domain. High spatial frequency errors can be considered a local property of the mirror surface, invariant under operations such as mounting and vibration testing. Therefore, these properties were measured only at the start of our process with a Topo2D micro-interferometer and are not discussed further here.

The initial 0g figure verification was a combination of three interferometric tests: a full-aperture horizontal test, a sub-aperture horizontal test, and a full-aperture vertical test. The measurement capabilities of these three tests overlap; however, each test provides unique information required to complete a full 0g figure verification.

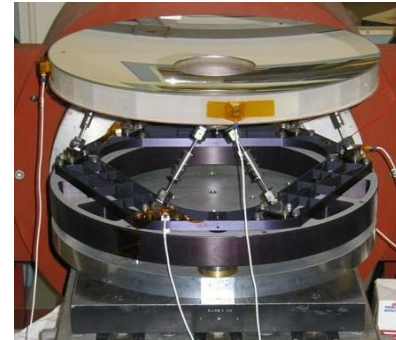
Sub-aperture and full-aperture auto-collimation tests were performed horizontally on the un-mounted mirror oriented in 24 positions rotated in 15° increments about the optical axis. This was accomplished with an in-house built quasi-kinematic metrology mount. The full-aperture horizontal measurements capture sag variations as the gravity vector rotates 360° in the plane normal to the optical axis. Ideally, this allows for the direct measurement of 1g sag, and therefore an accuracy assessment of the sag predictions and the fidelity of the finite element model (FEM). More pragmatically, the sag symmetry can provide data less sensitive to model uncertainties compared to data collected at a single mirror-to-gravity orientation. The sub-aperture measurements cover mid-spatial frequency bands where roughness measurements and full-aperture interferometry lack their full sensitivity.



Mirror mounted in horizontal metrology mount



Flight mounted mirror on the "tophat" metrology fixture.



Flight mounted mirror undergoing vibration testing at NASA's Wallops Flight Facility

Figure 2. The SHARPI/PICTURE primary in various test configurations (left to right): (a) horizontal testing, (b) vertical testing, mounted, and (c) vibration testing

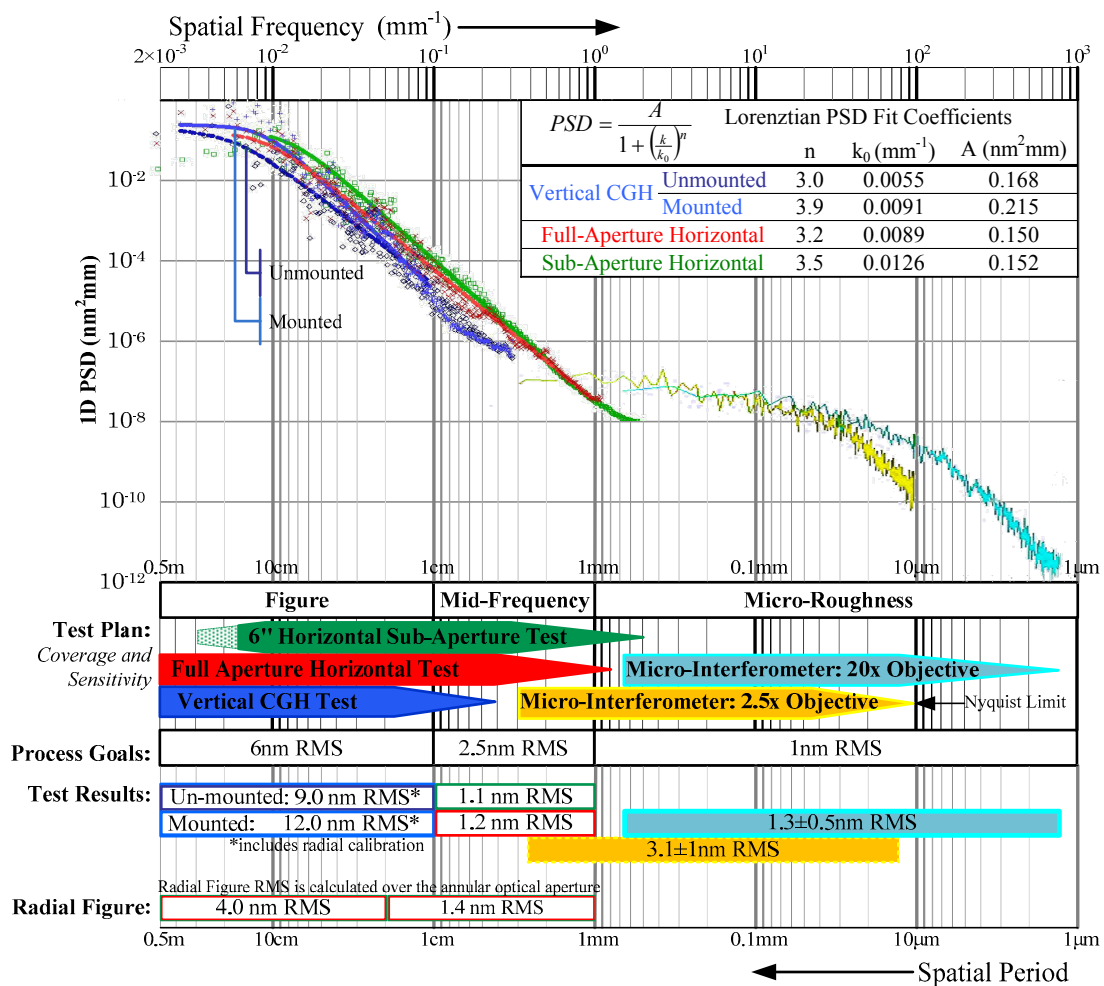


Figure 3. Initial mirror goals, measurement configurations, and results across the spatial frequency spectrum

The vertical mirror figure test was performed with a computer generated hologram (CGH) acting as a diffractive null. The vertical metrology delivered critical accuracy and precision from acceptance of the mirror through vibration qualification. Measurements at 12 different orientations offset by  $30^\circ$  were used to separate certain reference wavefront errors terms from the determination of mirror figure. With the combination of correct hardware, proper analysis, and a massive number of data points collected at a dozen different orientations, it was possible to resolve both the initial 9nm

RMS figure in a weightless environment (referred to as the “0g figure”) as well as changes as small as 1nm RMS associated with various mounting processes. A critical capability of the vertical test was the capability to measure the mirror in situ during mounting.

Data from the horizontal (See Fig. 2a) and vertical tests (Fig. 2b) are integrated to get a full picture of the 0g figure across the spatial frequency spectrum. The lateral spatial resolution of this test, 233 pixels over the 50cm clear aperture, was adequate to correlate measured data to various FEM cases; however, the ancillary horizontal tests were necessary to resolve higher spatial frequencies and their distribution. To aid the separation of reference wavefront error from the vertical measurements, data is extracted from the horizontal measurements and combined with data from the vertical measurements. The application of n-position wavefront algebra<sup>4,5</sup> to data from the vertical test decouples certain test wavefront terms from the measurement of the mirror figure error. However, an n-position test does not decouple the axisymmetric terms of the reference wavefront and the mirror figure, such as conic and spherical aberrations. For the calibration of the radial profile, the horizontal tests are used to measure the initial radial figure error, while the vertical CGH test can monitor any change in radial figure.

Throughout the program, the goal was to verify and maintain EUV-VIS diffraction limited performance for the intended spaceflight or “0g” environment or with an uncertainty at or below 2nm RMS.

## **4. HORIZONTAL FULL-APERTURE TESTING**

### **4.1 Motivation**

The n-position test allows for an accurate measurement of mirror figure features that are not symmetric under n-fold rotation<sup>4,5</sup>. The n-position test allows these terms to be separated and attributed to either the reference optics or the test optic. Axi-symmetric errors, invariant under any rotation, are inseparable between the reference optic and the test optic. To accurately attribute conic error, spherical aberration, or higher order radial figure terms, either the reference or test optic must be independently calibrated.

In this case, CGH fabrication errors or systematic piston error along the optical axis could mix with the conic or spherical aberration present in the mirror. Rather than qualifying the null optic, we chose to independently test the radial error using a large-aperture interferometer in an auto-collimating or “quad-pass” configuration. The reference wavefront from a 60cm aperture interferometer has been calibrated using stitched measurements of a 30cm NIST\*-calibrated<sup>5,6</sup> flat and cross-checked against a 50cm flat whose surface figure had been measured on several different instruments.

Mirror distortion due to gravity was modeled using a NASTRAN finite element model (FEM) and subtracted from the data. To mitigate the uncertainty in these distortion predictions, various mirror orientations were measured to exploit symmetry. Despite an unanticipated distortion of the mirror caused by mounting strain, an analysis of the measured distortion allowed for a separation of the 0g figure error such that the radial figure could be determined to within 2nm RMS over the aperture.

### **4.2 Layout and Hardware**

The test was performed with a 60cm aperture, wavelength shifting Fizeau interferometer. The horizontally collimated beam is brought to focus by the parabolic test optic and auto-reflected by a con-focal, high precision reference sphere. The test beam retraces its path, reflecting off the test optic again, returning to the interferometer. The metrology mount holds the mirror horizontally at three tooling balls affixed to evenly spaced mount pads on the mirror. The metrology fixture has a rotation bearing aligned to the optical axis with 24 pinned positions in 15° increments. The mirror and reference sphere are first aligned to minimize tilt, power, astigmatism, and coma. Once measurements conclude at a given orientation, the mirror is rotated 15° about the optical axis and realigned to the interferometer and reference sphere. A full set of measurements contains at least 5 nulled measurements at each of the 24 positions.

### **4.3 Analysis**

Using a detailed finite element model of the lightweight test optic, the expected surface figure distortion is calculated from 1g lateral loads when the mirror is constrained by the tooling ball interface. The wavefront error caused by the gravity sag prediction is subtracted at each position along with the interferometer’s calibrated wavefront. Given a mirror figure that is a linear function of loading, a pair of measurements where the gravity vector is rotated 180° should average

---

\* At the XCALIBIR<sup>7,8</sup> facility, run by Ulf Griesmann at the National Institutes of Standards and Technology (NIST)

to the 0g shape. Effects such as pupil shear, alignment, and numerical manipulation can affect the accuracy of this technique when gravity distortions are large. Therefore, modeled gravity distortion is first subtracted from the data and then the smaller modeling uncertainty is averaged out through the combination of symmetric orientations.

Three 6 mm diameter ink fiducials, placed at a radius of 254mm, are located in the intensity map of each measurement. The accurate location of these fiducials provides the centering, scaling, and orientation data that are required to correctly register the FEM gravity loading prediction and consolidate the measured data from the various orientations. Thorough fiducial registration produced a sub-pixel vertex location, an angular clocking uncertainty of  $\pm 6$  arc-min, and a pixel scale uncertainty  $\pm 0.1\%$ .

Once the test wavefront calibration and the gravity sag deformation are removed from the each phase measurement, each clocking orientation is rotated into a common frame and averaged. This generates the average wavefront error that co-rotates with the mirror.

Initial analysis of the reduced data indicated a much larger surface figure error than expected. From this test, the predicted 0g figure was 22.5nm RMS as compared to our later measurements of 9nm RMS. A series of FEM simulations, approximating the installation of the mirror into the metrology mount, produced a distortion prediction of similar shape and magnitude to the change in figure. Although the mirror was not over-constrained during its horizontal capture in the metrology mount, it had captured the strain of its own weight as the load was transferred from the un-mounted to mounted condition.

Without the means to correct the suspected problems with the mount process, the data was set aside as we built the vertical test, where a more standard kinematic mounting was possible. The vertical tower data confirmed the distortions present in the horizontal data were not intrinsic to the mirror and were most likely due to horizontal mounting stresses. However, the vertical test data was not an absolute measurement of axi-symmetric error, so the horizontal data was re-examined to see if conic errors and spherical aberration could be reduced from the distorted data.

Although the FEM approximation to the mount process showed a similar distortion to what was measured, the precise boundary conditions during the horizontal capture of mirror were unknown. A direct subtraction would be dominated by the difference between the modeled and actual boundary conditions. The asymmetric error is verified by the vertical n-position test, the data needed from this test is the low order radial profile – such as conic error or spherical aberration.

To decide whether usable radial figure information might be extracted from the measure data, two extremes were considered. In one extreme, the distortion of all possible captured strains could not introduce a radial shape change; therefore, the exact boundary conditions become irrelevant, and the measured average radial profile would be the actual radial profile. On the other extreme, if various interface conditions introduce strong radial shape changes, the relaxed radial figure error and the change in radial figure error due to captured strain would be inseparable. In the worst possible case, a radial figuring error in the unconstrained mirror would be hidden by the mechanical constraints, only to re-appear when the constraints were relieved. By analyzing the radial figure influence of possible captured strains, approximating the true radial figure or bounding the total error was possible.

Using FEM test cases, unit forces and torques were applied in each degree of freedom at each of the tooling ball interfaces with the assumption that the all other tooling ball interfaces were fixed. This produces 18 cases of possible mirror distortion. With some care, a reduced number of orthogonalized influence functions were produced. The low order Zernike terms (coupled with alignment error) and higher order spherical aberration terms were then subtracted from the orthogonalized influence functions. Given the assumption that the distortion present in the mirror could be closely approximated by a summation of forces applied at the tooling ball interface, the combined basis set would then span the space of possible alignment error, induced distortion, and spherical aberration. Fitting the measured data to this basis set produced a residual closely matching the expected surface figure.

The initial 18 test cases were fit to this basis set. Various combinations of these test cases that produced the measured fit coefficients were derived. A set of cases that reproduced the observed basis coefficients using the least input force and torque were assembled. In that set of solutions, two 5in-lb torques applied at mount interfaces could explain over 90% of the observed 22nm RMS distortion. This case was well within the range of possible conditions during the mounting procedure. A wide set of input force and torque solutions were examined. These solutions matched the magnitudes of the measured orthogonalized distortion coefficients and were not optimized or selected based on their agreement with the remaining coefficients. No member of the solution set was found to contribute more than 1.5nm RMS of 3<sup>rd</sup> order spherical aberration. Interestingly, all solutions explored in the solution set matched the 2nm RMS 5<sup>th</sup> order spherical

aberration observed within  $\pm 0.5\text{nm}$  RMS even though matching the spherical aberration terms was not part of the fit optimization or the selection of possible cases. This suggests that the  $2\text{nm}$  RMS of 5<sup>th</sup> order spherical aberration was mostly a result of the captured strain – a result that was insensitive to the particular conditions at the interface that caused the observed strain.

Using actual input force/torque solutions from a solution subset, distortions were reconstructed and compared to the estimated distortion from the orthonormal (plus alignment) basis used for fitting the measured data. The residual between the “real” cases, as calculated by a combination of the 18 test cases, and the orthonormal distortion fit were below  $1\text{nm}$  RMS. These residuals consisted of higher spatial frequency details than were of interest in the radial profile. The calculated distortion was then subtracted from the figure measurement to produce the expected un-strained figure.

The result matched qualitatively with both vendor supplied data and our rigorous un-mounted measurements from the vertical test tower. Quantitatively, the  $8.2\text{nm}$  RMS  $0g$  “un distorted” estimate is lower than the finally reduced  $9\text{nm}$  RMS figure of the un-mounted mirror measured facing vertically. This is expected because some of the initial mirror figure was a result of the adhesive cure on the mount pads, and that shape term mixed with the 18 initial FEM test cases. Therefore, the distortion solution included some of this small effect.

## Horizontal Full-Aperture Measurement Decomposition

The measured and reduced figure from the horizontal measurement contains distortion from the metrology mount. Solving for and subtracting those distortions generates the un-strained  $0g$  figure. To validate this subtraction, data from a kinematic condition is compared to the solution, producing a  $4.9\text{nm}$  RMS residual.

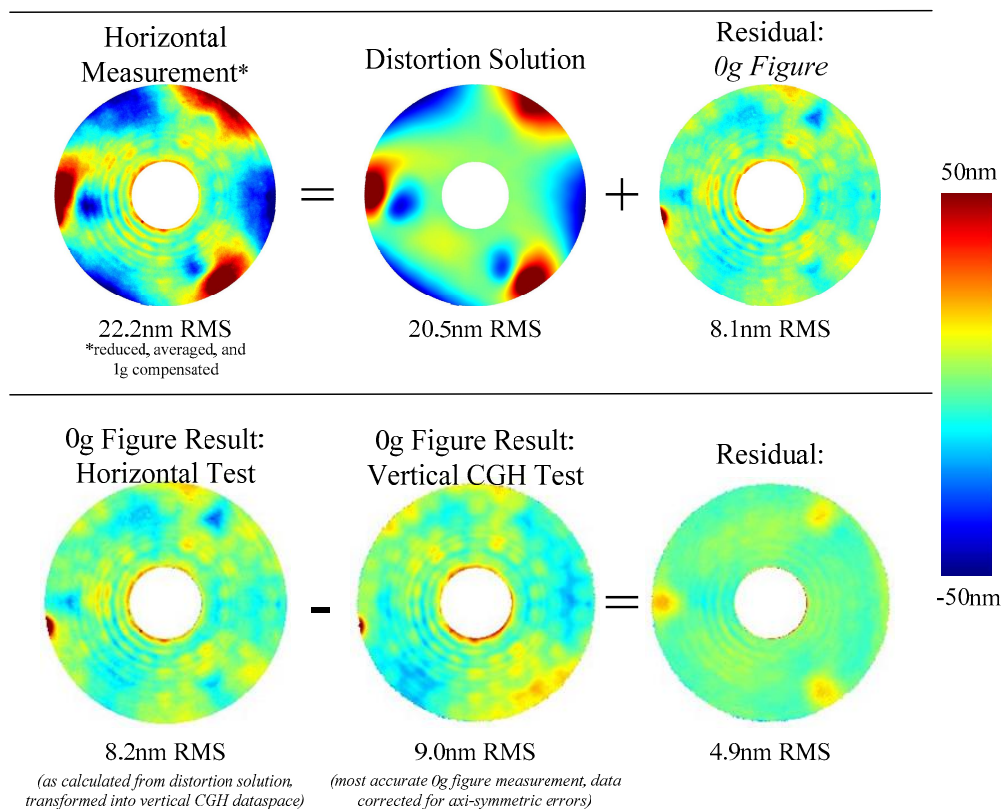


Figure 4. Figure distortion decomposition and residual from horizontal full-aperture metrology

### 4.4 Summary of Horizontal Full-Aperture Interferometry

The full-aperture horizontal metrology indicated a significant amount of mirror figure distortion. The shape and magnitude of this distortion matched FEM predictions of distortion resulting from capturing strain during the process of mounting the mirror in its horizontal metrology mount. Without knowledge of the exact boundary conditions during the





The sub-aperture measurements produce an integrated RMS in the mid-spatial frequency band of 1.1nm RMS. A similar calculation using the full-aperture horizontal data produces 1.2nm RMS.

In addition to measuring integrated mid-spatial frequency error, radial error in the 1mm-10mm spatial period band was determined. This was made possible by an accurate determination of the parent vertex in interferometer pixel-space. Once radial coordinates are determined, average radial profiles over the inner ring and the outer ring are calculated. Given the 0.28 mm/pixel scale, and the location of the parent vertex to less than one pixel, the average radial profiles derived from the inner and outer ring are heavily averaged and well resolved to less than 1mm.

## Total Radial Profile Derived from the Low Frequency Radial Figure and the High Frequency Radial Figure

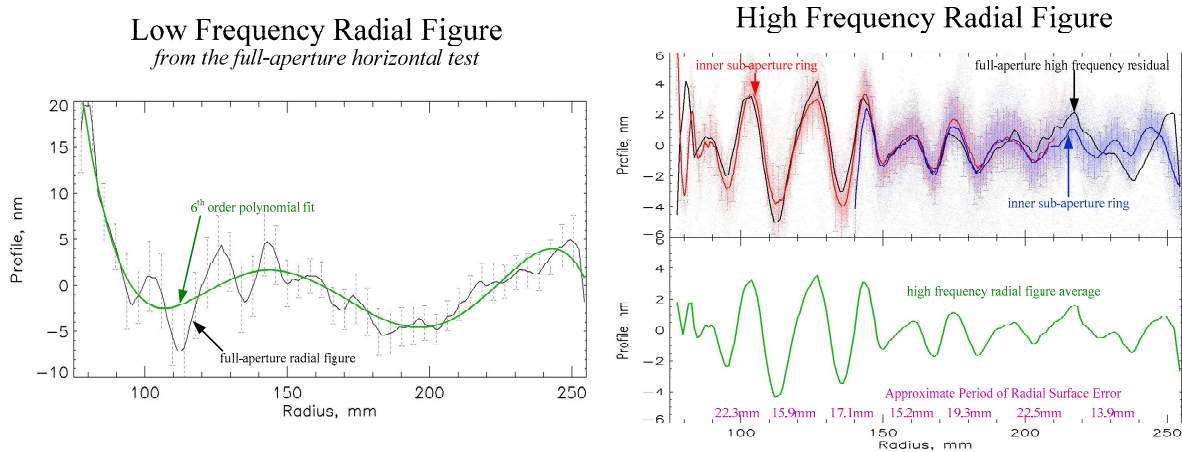


Figure 6. Low and high spatial frequency components of the radial profile.

## CGH Radial Figure Correction using the Total Radial Figure

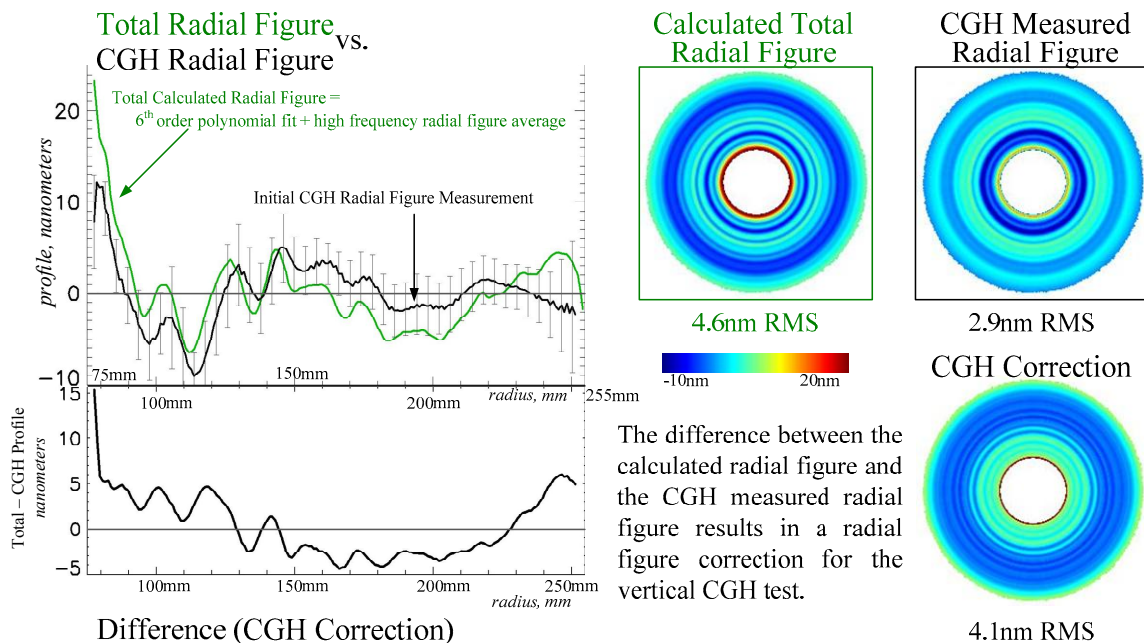


Figure 7. Total radial profile, radial figure as measured with the CGH, and radial figure correction to CGH measurements.



To create an accurate radial profile, a combination of the full-aperture radial profile and sub-aperture radial profiles are used. To capture the large scale radial shape, a sixth order polynomial is fit to the full-aperture data (Fig. 6, on left). The residual to this fit shows the smaller scale ripples present in the full aperture data. By combining the well matched sub-aperture profiles with the residual to the full-aperture radial profile fit, a higher resolution radial profile is calculated (shown on the right of Fig. 6). The total radial profile is then calculated by adding the polynomial fit to the averaged profile (Fig. 7). The agreement between this independently measured radial profile and the radial figure measured from the n-position vertical CGH null test is approximately 4.1nm RMS. The main components of this radial difference are 3.7nm RMS of 3rd order spherical aberration and 2.2nm RMS of higher frequency, un-resolved radial errors. The lower resolution of the vertical CGH test missed the sharpness of the roll-off error at the inner radius.

## 6. VERTICAL TEST

### 6.1 Technical Approach: Design, Alignment, Environment, Data Collection, and Data Analysis

In the vertical test setup (Fig. 8), a Computer Generated Hologram (CGH) acts as the diffractive equivalent of an Offner null lens. The null lens is used to introduce aspheric departure in the spherical test wavefront to match the parabolic mirror. The Diffraction International CGH is certified to 6nm RMS; however, by exploiting symmetry and n-position testing, we are able to reach accuracies approaching 1nm RMS. Although accurate radial figure error is not calibrated by the n-position measurement scheme, the measured change in mirror's radial figure is accurate throughout the stages of testing given the measured stability of our reference wavefront. A central motivation for vertical testing was to allow measurement of changes in surface figure through mounting and mirror processing. The initial radial figure calibration in combination with the n-position test, therefore, eliminates our need to verify the reference wavefront, that is, the combination of the null lens and spherical transmission lens.

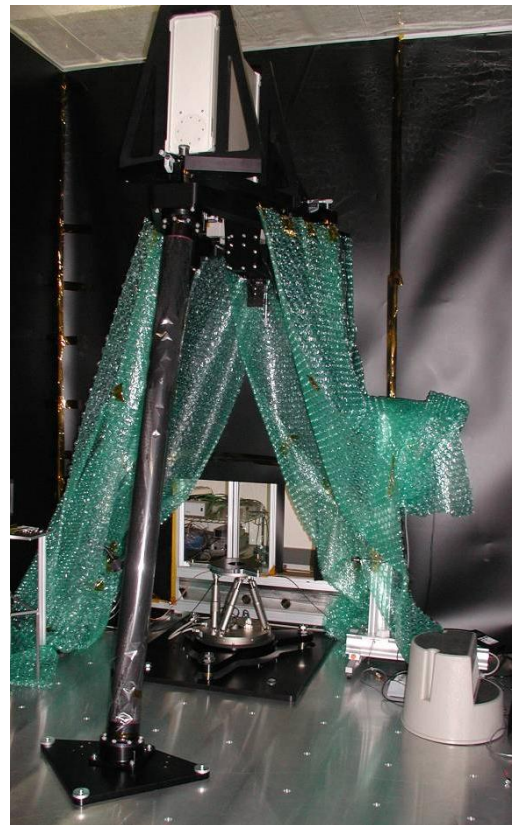
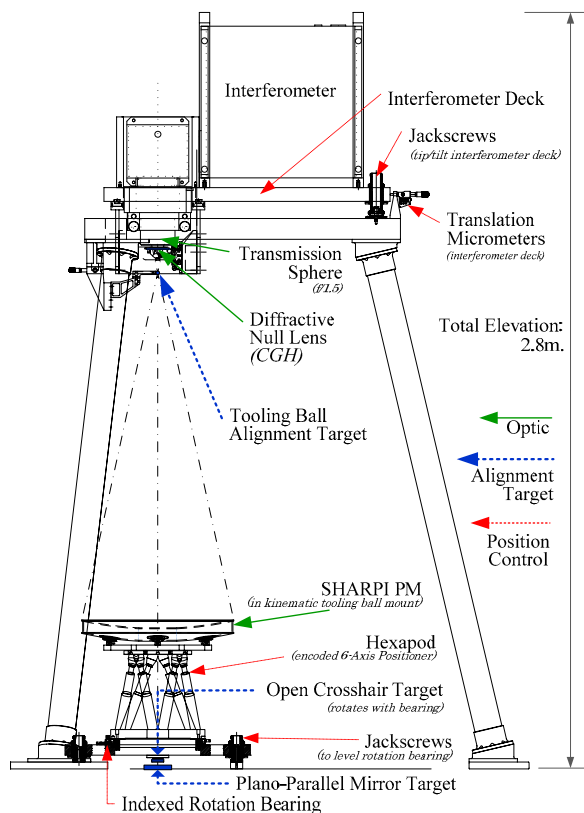


Figure 8. Vertical test tower diagram (left) and vertical test tower with kinematic mount platform.

## Addition of Radial Figure Correction to CGH Measured Figure Error

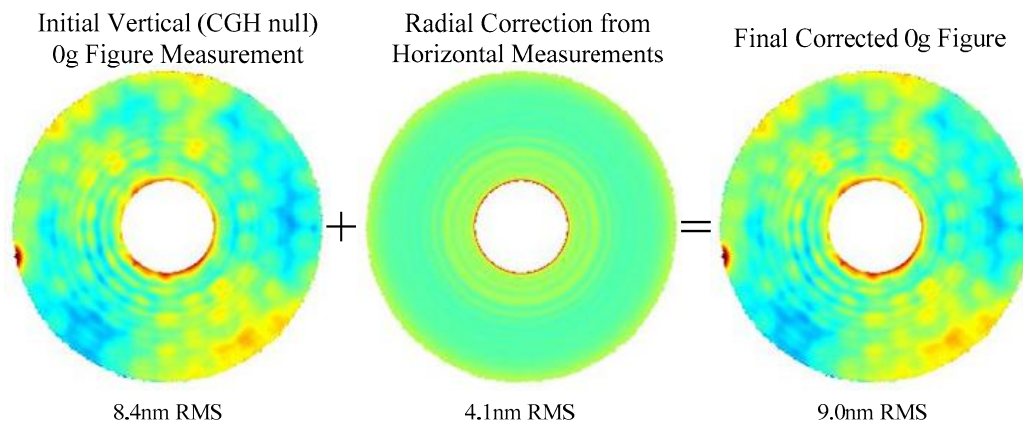


Figure 9. Radial figure correction applied to vertical CGH metrology.

To perform an n-position test, figure measurements are taken with the mirror in various orientations about the optical axis. By tracking the features that rotate with the mirror, the rotationally asymmetric errors can be determined, up to an angular period limited by the number of positions. The mirror must be staged so that it can be rotated and realigned quickly relative to the initial system alignment. We placed an encoded 6-DOF hexapod on a high class rotation bearing and aligned the axis of the bearing to the optical axis. To perform this alignment, an optical plummet was used to auto-collimate and center a plano-parallel mirror under the rotation bearing, an open-crosshair at the center of the bearing, a tooling ball aligned to transmission sphere's focus, and a the back of the CGH. The interferometer and CGH were positioned so that the retro-null alignment feature of the CGH, visible to the interferometer, was aligned in parallel with the optical plummet targets. Optical elements, staging, and alignment targets are shown in Figure 8.

A tent was required to reduce temperature variations and air currents. The tent structure around the entire tower worked efficiently at reducing the temperature variations; however, the vertical temperature gradient and air currents were still unacceptable. A second enclosure was placed around the optical path, supported from the tower structure itself. A fan inside the large tent, but outside the smaller enclosure, helped mix the air and reduce thermal gradients while the secondary enclosure shielded the optical path from air currents. The center obscuration of the mirror was plugged with material to avoid air convection through the central hole of the mirror. In the end, the thermal stability supported nanometer-level metrology. The bulk temperature within the secondary enclosure was  $18.5^{\circ}\text{C} \pm 0.25^{\circ}\text{C}$ , the vertical temperature gradient over 2.5m averaged  $0.2^{\circ}\text{C} \pm 0.1^{\circ}\text{C}$ . Both the bulk temperature and gradient oscillated with two main frequencies: a 60min period corresponding to climate controls as well as a diurnal cycle. The order in which the mirror was rotated about its axis and measured was chosen to mitigate any systematic error from this temperature cycling.

Once the tower, bearing, and CGH axis are aligned, fine alignment is performed with the hexapod. Using the hexapod's encoder, the mirror is iteratively aligned by regressing previous location/aberration pairs until drift or hexapod movement resolution becomes the limit to alignment. A measurement set is started when the cavity is nulled to less than 2 arc-sec in tilt and no coma or power errors RSS-ing to more than 30nm RMS over the aperture. Automated measurement would proceed until these criteria were exceeded by a factor of two. On average, once initial alignment was reached, 10-20 additional re-alignment steps would produce 100 datasets meeting alignment criteria. For a full rotation dataset, at least 100 measurements are taken at each of the 12 bearing positions.

Once a rotation is complete, the fiducial locations are registered in the data using multiple images from each position. Centering, scaling, and rotation data are extracted and used to rotate the data at each position into a common frame, remap the distorted pupil into linear space, and subtract the gravity sag. The measurement and analysis was repeated with various mirror orientations and different camera resolutions and was repeated at many steps during the mounting process. On average, the repeatability of the derived 0g surface figure error from a full dataset was 1.0-2.0nm RMS. After the radial figure correction from the horizontal tests described in sections 4 and 5, the initial figure error measured to spatial periods as low as 5mm was 9.0nm RMS.

## 6.2 Mounting

The first step in our mounting procedure was to attach the socket end of a ball and socket joint to the mirror mount pads. Each socket was held to the invar mount pad with one #8 screw tightened to 35 in-lb, and one of the bipod legs is attached to each socket. After completing this step, we repeated a set of figure measurements that indicated the figure error had increased to 30nm RMS. To confirm that the torque value of the screw was responsible for the distortion, we first ran a NASTRAN simulation with boundary conditions that estimated this torque value. The FEM result was similar to the measured distortion. Furthermore, we loosened the #8 screws, and the mirror relaxed back into its original shape.

The screws held a critical joint in the load path between the mount ring and the mirror. It was necessary to find a preload large enough to be acceptable for flight survival but still small enough to avoid major mirror distortion. Because of the length of the measurement cycle and the increased risk to hardware, we could not perform an exhaustive or stepwise search to determine the acceptable preload.

An orthogonal basis was created for fitting these measurements starting with the low order Zernike polynomial terms corresponding to tilt, astigmatism, power, coma, and spherical aberration. As these functions were already orthonormal (in a continuous sense), these Zernike components were removed from the NASTRAN-generated preload distortions. With some care, the selected Zernike terms were orthonormalized along with the FEM screw distortion cases as interpolated in the interferometric data coordinates (example basis functions are shown in Fig. 9). With this basis, we were able to assess the figure distortion as a function of actual applied preload. After applying a few torque levels and taking figure measurements at each value, the input torque was correlated to orthonormalized distortion coefficients. With this information, it was possible to quantify the torque value versus surface figure distortion tradeoff. All six screws were torqued to the decided level, and the measured distortion contribution from this effect was within 1nm RMS of the expected value.

The next mounting step involved rigidizing the bipod mount. The metrology and mount hardware were designed to enable interferometry at various steps during the rigidization process. Although we were unable to perform any mirror alignment during this process, the data still provided valuable information that help diagnose and correct a source of captured strain.

After the mount had been mechanically locked, we transferred the mounted mirror to a fixture allowing for a complete set of figure measurements (Fig. 1c) before finally bonding the mount. This gave us a chance, albeit risky, to unlock the mount and re-try the mounting procedure. This metrology required a special adapter to hold the mounted mirror on the hexapod while maintaining the same the mirror vertex elevation. Due to the shape of this fixture, we referred to it as the “top hat” fixture.

The first measurements on this “top hat” fixture revealed more than 25nm RMS astigmatism. During the rigidization process, the in situ data collected contained large variations in tilt, focus, and to a lesser extent coma; however, the in situ mounting data did not indicate the magnitude of astigmatism present in the top hat measurement. Additionally, it was curious that a fairly uniform astigmatic shape could be produced by a mount and interface geometry that was 3-fold symmetric.

Given the extraordinary sensitivities of this mirror, we suspected that if the mirror mount deck was placed on a support plate that had a mechanically insignificant astigmatic shape, then the slight compliance of the mount deck over this shape due to its own weight would be sufficient to enforce an astigmatic shape on the mirror surface. By analogy, if the brim (i.e. the surface that the mirror deck rested on) of the top hat was curled rather than a flat, the compliance of the base of the mirror mount might cause the observed astigmatism in the mirror.

We adapted the n-position procedure to include these  $3 \times 120^\circ$  permutations of the mount to fixture orientation, such that  $4 \times 90^\circ$  orientations were taken at each of the  $3 \times 120^\circ$  mount to fixture permutations. The geometry produces 12 unique reference wavefront to optic orientations. Adding an additional layer of wavefront algebra allowed for the separation of the reference wavefront, mirror figure, and the effect of the tophat fixture.

This wavefront analysis indicated that 10nm RMS of the astigmatism was attributable to the tophat fixture whereas 15nm RMS astigmatism was, in fact, present in the mirror. With the decomposition, a localized mirror distortion became more evident. A stress around the mount pads was contributing 8nm RMS surface figure error.

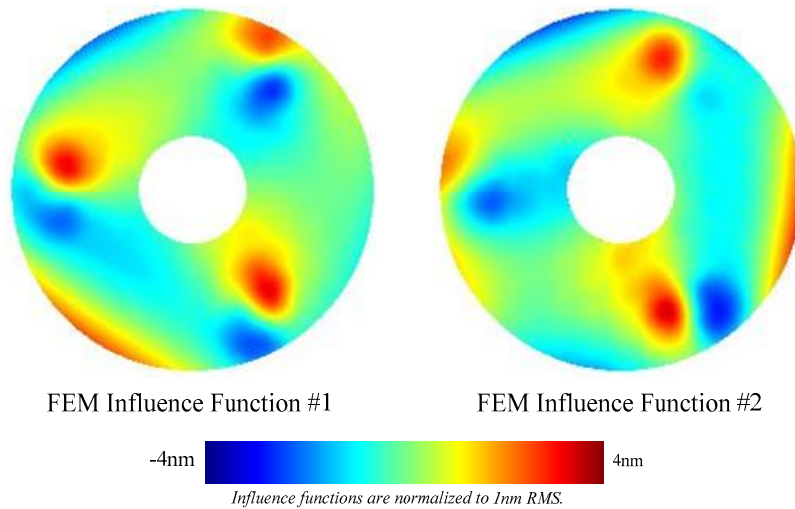
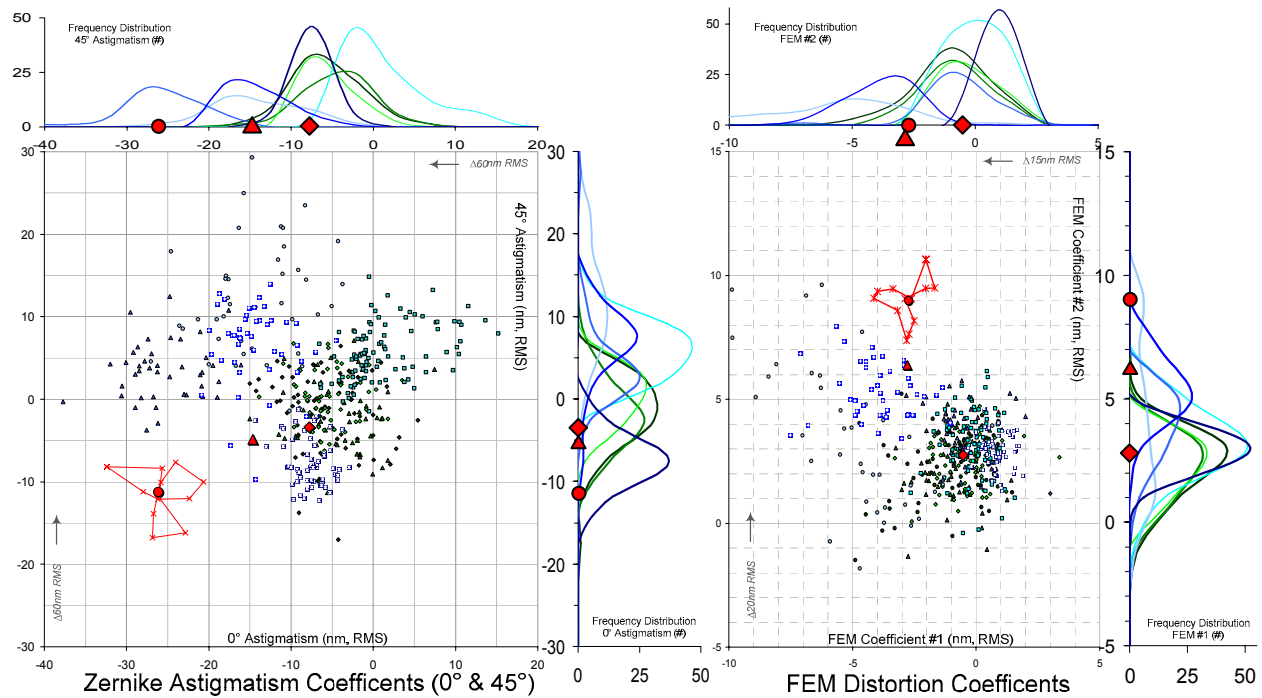


Figure 10. FEM 1 and 2: Two orthonormalized influence functions derived from FEM distortion cases. These shapes showed a significant change through the mounting process.



- ◆ Step 1 (loose)
- ▲ Step 2 (tighten)
- Step 3 (tighten)
- Step 4 (loosen)
- Step 5 (tighten)
- ▲ Step 6 (locked)
- Step 7 (remove support)
- Step 8 (unbolt)
- ✖ n-asphere set (12×30°)
- Average n-asphere set
- ▲ 3×4 n-asphere mount compensation
- ◆ Final mounted condition

These scatter and distribution charts show the coefficients of 3<sup>rd</sup> order astigmatism and two of the FEM basis functions. The scatter data are taken during the process of mechanically locking the mirror mount (steps #1-#8) when no realignment is possible. The mirror was then transferred to a metrology mount and measured at 12×30° clocking increments. The closed loop structure indicates that the distortion co-rotates with the mirror. The measured figure error was now far from diffraction limited at visible wavelengths. The error included a large amount of astigmatism and additional higher order distortion. ●

To determine if the figure change was due to the metrology mount or captured strain from mounting, 3×120° mount-to-mirror orientations were tested at 4×90° increments (3×4 n-position). Results were analyzed to remove the effect of the metrology mount. ▲ This analysis showed that the metrology mount was a significant source of the new astigmatism. However, the remaining change to the 0g figure was significant, particularly in the FEM basis functions. We were able to identify both the metrology mount as a source of distortion and the captured strain from the mounting process. The correlation between the FEM basis and various FEM cases informed our successful plan to release the captured strain remaining in the mirror. After which, both astigmatism and FEM values returned to near-premount values. ◆

Figure 11: Astigmatism and FEM coefficient values during and after mounting

The mirror mount deck was bolted to an assembly ring during the rigidization of the mount. Even though the interface to the assembly ring was precision lapped, the mirror deck would have been forced to conform to any non-uniformity in the assembly ring as it was bolted down. Once released, the mirror deck could relax and transmit the captured strain present in the bent mirror deck through the bipods into the mirror.

To correct this problem, we needed to a procedure that could release energy stored in a deflected mirror deck. By loosening a subset of the bipod joints, the mount assembly could relax, and then the joints could be re-tightened. To perform this operation without capturing more strain in the mirror, we positioned and balancing the mirror carefully using the hexapod and interferometer and took pains not to disturb that condition through the process.

After this procedure, measurements indicated that mirror had relaxed. The change in astigmatism had been reduced to 7nm RMS, and the 8nm RMS local distortion was reduced below 2.7nm RMS. All joints were then bonded in place. After the adhesive had cured, we took a full set of measurements. The mounted mirror was then taken to Goddard's Wallops Flight Facility for vibration testing. After returning, a the mirror underwent another round of testing. In total, the final mirror figure was 12.5nm RMS as compared to the initial figure of 9nm RMS.

Most of the figure change from our entire process (8.8nm RMS) was attributed to the expected distortion from the fasteners attached to the mount pad. There was a 7nm RMS change in astigmatism, which was likely the combination of the troublesome fasteners and the remaining captured strain from rigidization of the mount. The remaining effects from the process were calculated to be under 4.5nm RMS. Measurements before and after vibration showed no change in mirror figure greater than 1nm RMS, our measurement uncertainty. Figure 11 shows some of the astigmatism and FEM distortion coefficients through the mounting process. Figure 12 show the final mirror figure and its change from its pre-mount figure. Total radial figure change through this process is shown in Figure 13. Figure 14 compares the measured figure change relative to the expected distortion from the mount pad screws, and a summary decomposition of mirror figure changes is shown in Figure 15.

## Total Figure Change:

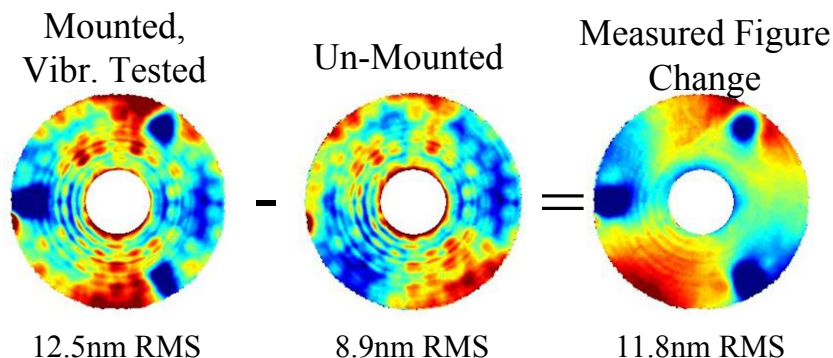


Figure 12: Change in mirror surface figure from un-mounted to the mounted and vibration tested.

## Change in Radial Profile: from Initial to Post-Mount and Vibe Measurement

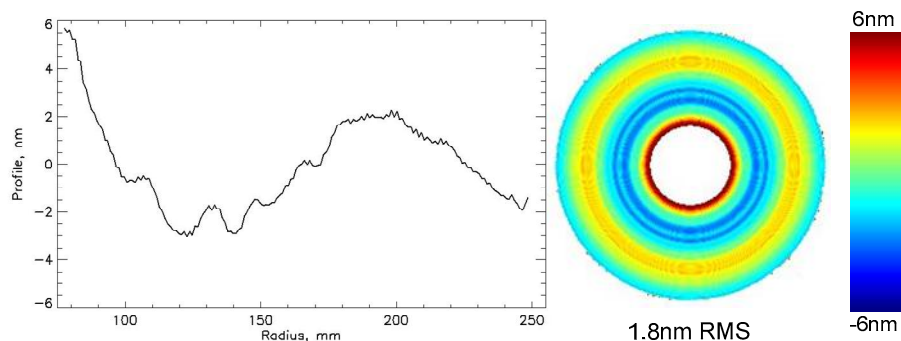


Figure 14. Changes in radial figure from pre-to-post mount.



## Decomposed Figure Change: Measured and Expected

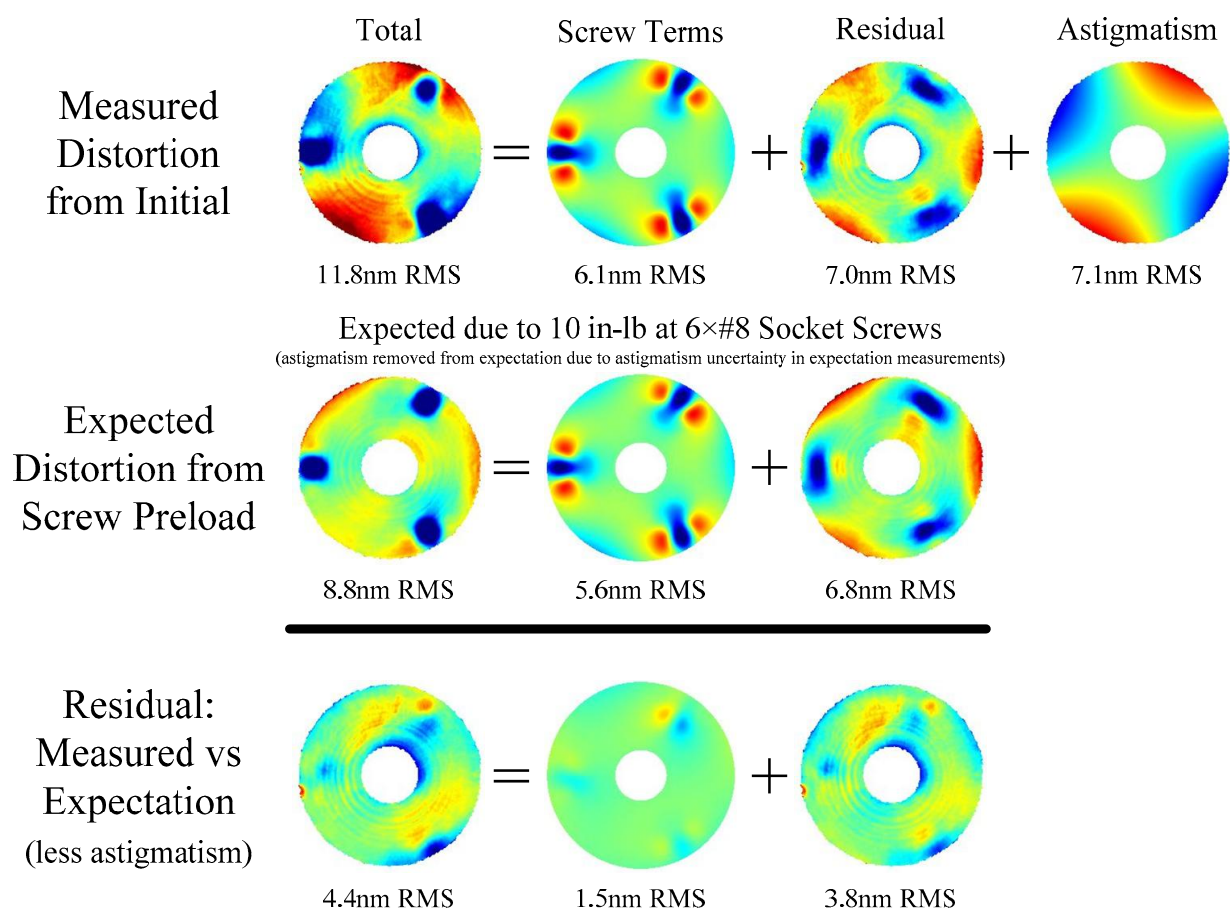


Figure 13: The expected distortion contribution from the torque values of the mounting pad screws

## Accounting for Changes in Mirror Figure:

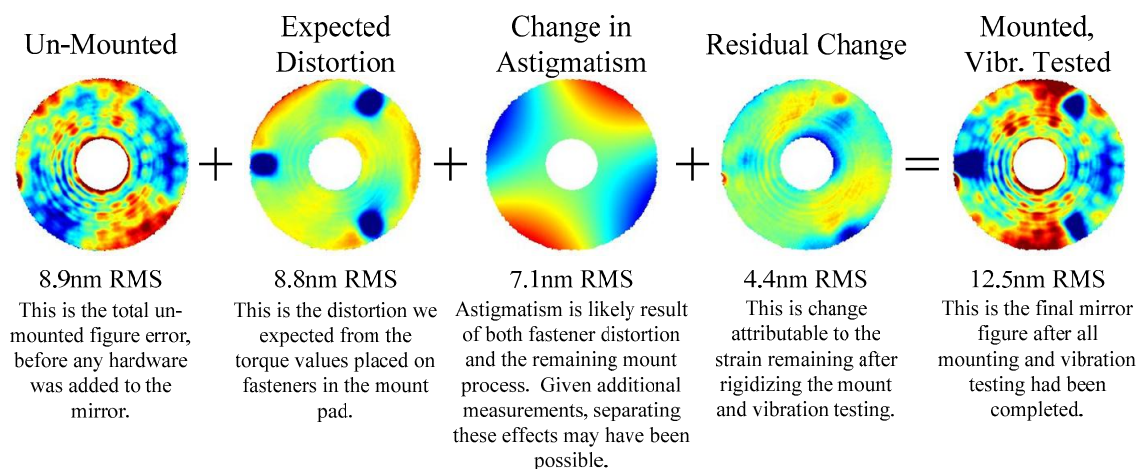


Figure 15. A decomposition of the changes in mirror figure from pre-to-post mounting.

## 7. CONCLUSION

Perhaps the largest obstacle in the high accuracy, 0g verification of a lightweight optic is the measurement and compensation for the deflection of the optic under its own weight. Diffraction limited performance is desired in operational 0g environment. Given the size of an optic and the degree to which stiffness has been reduced from the lightweighting process, the differential between the 1g shape and the relaxed 0g shape can be a significant factor in achieving diffraction limited performance on orbit. Subtracting the expected gravity distortion under the modeled metrology conditions or implementing a mechanism to offload gravity during measurement present their own set of technical difficulties and uncertainties. Additionally, mounting the optic so that it can survive flight loads, or even just to accomplish the metrology, requires mechanical constraints that become potential sources of mirror distortion. If the expected gravity sag is large compared to 0g requirements, the distortion due to mechanical constraint becomes a small fraction of the expected 1g shape. However, in the operational 0g environment, the potentially significant mechanical distortion remains. For this lightweight mirror, after the subtraction of a change in curvature, the gravity sag measures 310nm peak-to-valley and is 75nm RMS, as compared to the calculated initial 0g mirror figure error of 9.0nm RMS. Despite this gravity distortion as well as significant mount induced distortions, we were able to use finite element models and various analysis techniques to successfully use data that contained these effects to discern nanometer RMS sized features that would remain in the 0g figure. Compared to testing in the operational environment, there are more details that require attention and more potential pitfalls; however, given an accurate mechanical model of the optic, certain analysis techniques can make this task manageable.

Some firsts on this program (to our knowledge) include: the first CGH accuracy certification to  $\leq 2$  nm rms; the first absolute test of an aggressively lightweighted asphere to  $\leq 2$  nm rms; the first verification of gravity sag model to  $\leq 2$  nm rms; the first ultra-lightweight, high-precision, mounted 0.5m mirror measured to maintain its figure after exposure to a launch environment comparable to those found on orbital and sounding rocket vehicles.

## ACKNOWLEDGEMENTS

This project was made possible by Internal Research and Development funds through NASA Goddard Spaceflight Center as well as some funding from the PICTURE rocket program. We thank J. Gum and the Goddard coating team for performing both the metrology and flight coatings. We thank J. Bolognese and S. Irish for extensive finite element modeling. We appreciate the significant IR&D investment that ITT has put into the completion and polishing of this mirror as well as the subsequent support. Additionally, R. Keski-Kuha, T. Saha, and J. Davila at NASA/Goddard contributed significantly to the completion of the lightweight mirror demonstrator. Many thanks to those at the NASA/GSFC Wallops Flight Facility who provided support for vibration testing, and a special thanks to all those who helped collect the enormous volumes of test data that made this work possible.

## REFERENCES

- [1] S. Antonille, D. Content, D. Rabin, T. Wallace, and C. Stevens, "High Precision Metrology on the Ultra-lightweight UV 50.8cm f/1.25 parabolic SHARPI primary mirror," Proc. SPIE 5494, 132-140 (2004).
- [2] D. Rabin, J. Davila, D. Content, R. Keski-Kuha, and S. Michael, "SHARPI: Solar High Angular Resolution Photometric Imager," Bulletin of the American Astronomical Society: AAS 200th meeting, 34, 735- (2002).
- [3] M. Shao, J. K. Wallace, B. M. Levine, D. T. Liu, "Visible Nulling Interferometer," Proc. SPIE 5487, 1296-1303 (2004).
- [4] C. Evans and R. Kestner, "Test Optics Error Removal," Appl. Opt. 35, 1015- (1996).
- [5] C. Ai and J. C. Wyant, "Absolute testing of flats by using even and odd functions," Appl. Opt. 32, 4698-4705 (1993).
- [6] Robert E. Parks, Lianzhen Shao, and Chris J. Evans, "Pixel-based absolute topography test for three flats," Appl. Opt. 37, 5951-5956 (1998).
- [7] U. Griesmann, Q. Wang, and J. Soons, "Three-flat tests including mounting-induced deformations," Optical Engineering 46 (9), 093601-1 (2007).
- [8] U. Griesmann, Q. Wang, J. Soons, and R. Carakos, "A simple ball averager for reference sphere calibrations," Proc. SPIE 5869, (2005).
- [9] U. Griesmann, "Three-flat test solutions based on simple mirror symmetry," Appl. Opt. 45, 5856-5865 (2006).